

UvA-DARE (Digital Academic Repository)

Coexisting Charge-Ordered States with Distinct Driving Mechanisms in Monolayer VSe₂

Chua, R.; Henke, J.; Saha, S.; Huang, Y.; Gou, J.; He, X.; Das, T.; Van Wezel, J.; Soumyanarayanan, A.; Wee, A.T.S.

DOI

[10.1021/acsnano.1c08304](https://doi.org/10.1021/acsnano.1c08304)

Publication date

2022

Document Version

Final published version

Published in

ACS Nano

License

Article 25fa Dutch Copyright Act

[Link to publication](#)

Citation for published version (APA):

Chua, R., Henke, J., Saha, S., Huang, Y., Gou, J., He, X., Das, T., Van Wezel, J., Soumyanarayanan, A., & Wee, A. T. S. (2022). Coexisting Charge-Ordered States with Distinct Driving Mechanisms in Monolayer VSe₂. *ACS Nano*, *16*(1), 783-791. <https://doi.org/10.1021/acsnano.1c08304>

General rights

It is not permitted to download or to forward/distribute the text or part of it without the consent of the author(s) and/or copyright holder(s), other than for strictly personal, individual use, unless the work is under an open content license (like Creative Commons).

Disclaimer/Complaints regulations

If you believe that digital publication of certain material infringes any of your rights or (privacy) interests, please let the Library know, stating your reasons. In case of a legitimate complaint, the Library will make the material inaccessible and/or remove it from the website. Please Ask the Library: <https://uba.uva.nl/en/contact>, or a letter to: Library of the University of Amsterdam, Secretariat, Singel 425, 1012 WP Amsterdam, The Netherlands. You will be contacted as soon as possible.

UvA-DARE is a service provided by the library of the University of Amsterdam (<https://dare.uva.nl>)

Coexisting Charge-Ordered States with Distinct Driving Mechanisms in Monolayer VSe₂

Rebekah Chua,[¶] Jans Henke,[¶] Surabhi Saha, Yuli Huang, Jian Gou, Xiaoyue He, Tanmoy Das, Jasper van Wezel,^{*} Anjan Soumyanarayanan,^{*} and Andrew T. S. Wee^{*}



Cite This: *ACS Nano* 2022, 16, 783–791



Read Online

ACCESS |



Metrics & More



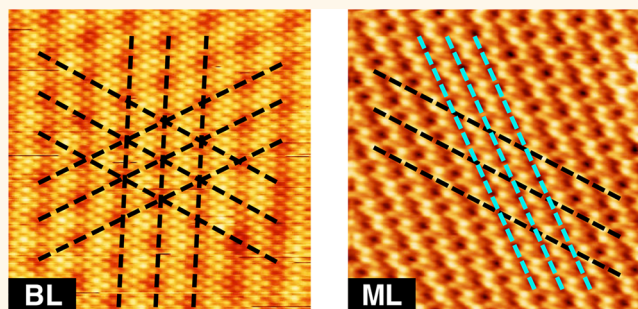
Article Recommendations



Supporting Information

ABSTRACT: Thinning crystalline materials to two dimensions (2D) creates a rich playground for electronic phases, including charge, spin, superconducting, and topological order. Bulk materials hosting charge density waves (CDWs), when reduced to ultrathin films, have shown CDW enhancement and tunability. However, charge order confined to only 2D remains elusive. Here we report a distinct charge ordered state emerging in the monolayer limit of 1T-VSe₂. Systematic scanning tunneling microscopy experiments reveal that bilayer VSe₂ largely retains the bulk electronic structure, hosting a tridirectional CDW. However, monolayer VSe₂—consistently across distinct substrates—exhibits a dimensional crossover, hosting two CDWs with distinct wavelengths and transition temperatures. Electronic structure calculations reveal that while one CDW is bulk-like and arises from the well-known Peierls mechanism, the other is decidedly unconventional. The observed CDW-lattice decoupling and the emergence of a flat band suggest that the second CDW could arise from enhanced electron–electron interactions in the 2D limit. These findings establish monolayer–VSe₂ as a host of coexisting charge orders with distinct origins, and enable the tailoring of electronic phenomena via emergent interactions in 2D materials.

KEYWORDS: two-dimensional materials, transition metal dichalcogenides, monolayer, VSe₂, charge density waves, scanning tunneling microscopy, band structure



INTRODUCTION

Charge order in crystalline materials typically manifests as a static modulation of electron density, known as a charge-density wave (CDW), accompanied by periodic modulations of the atomic lattice.¹ The prototypical CDW arises in (quasi)-one-dimensional (1D) systems from the “nesting” of parallel Fermi surface (FS) regions connected by the CDW propagation vector Q_{CDW} . As real materials do not exhibit perfect nesting, CDW formation is supported by either electron–phonon coupling (EPC), other collective excitations, or electron–electron interactions.^{2–7} In layered materials, CDWs often exist in proximity to other ordered phases, for example, superconductivity and magnetism,⁸ due to a precarious balance between competing interactions. Approaching the two-dimensional (2D) limit enhances the potential for such interplay,⁹ while providing new knobs to tune electronic phases, such as electric fields and strain.^{10–13} Notably, electron–electron interactions in the 2D limit are expected to induce competition among different CDW driving

mechanisms as well as other ordered states.^{14–16} In practice, however, a crossover toward electronic charge order driven by dimensional reduction remains to be discovered.

Transition metal dichalcogenides (TMDCs) are well-studied hosts of conventional and unconventional CDWs.^{4–6,8,17} The tunability of CDWs in the ultrathin limit of several TMDCs is particularly relevant to practical electronic applications.^{11–13,18,19} 1T-VSe₂ is a prototypical metallic TMDC with layered hexagonal crystal structure (Figure 1a). Bulk 1T-VSe₂ is paramagnetic, with a three-dimensional (3D) FS. Below temperature $T_{\text{CDW}}^{\text{bulk}} \sim 110$ K, it hosts a triple- Q (triangular) CDW with 3D character. The CDW periodicity

Received: September 21, 2021

Accepted: December 15, 2021

Published: December 21, 2021



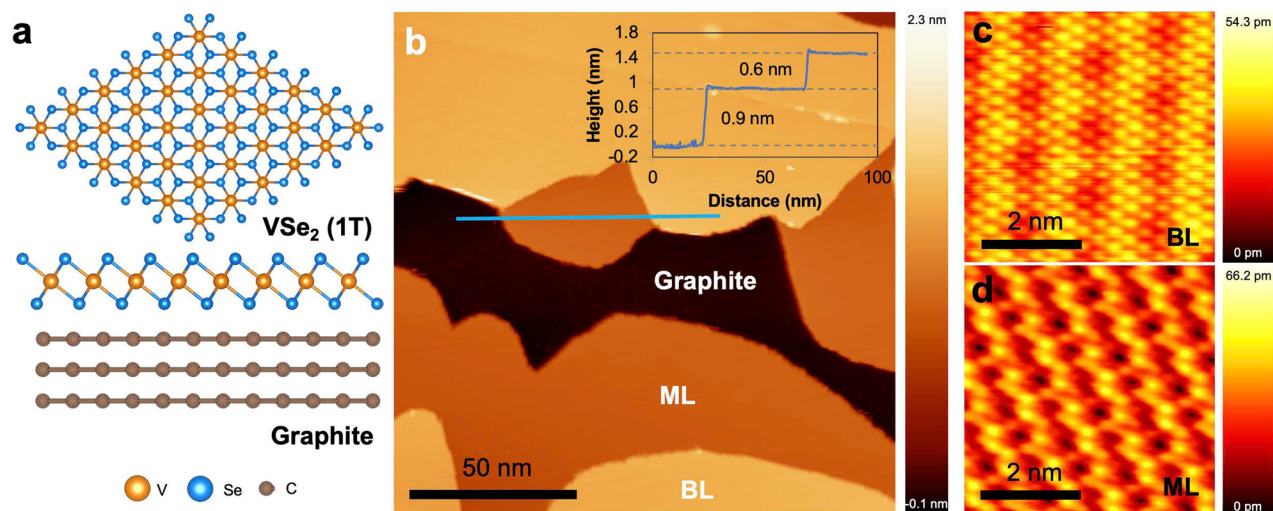


Figure 1. Crystal structure and STM Imaging of Ultrathin VSe₂. (a) Top view (top) and side view (bottom) of the atomic structure of 1T-VSe₂ on graphite substrate. (b) Large field-of-view STM topograph (150 × 150 nm², bias voltage, $V_{\text{tip}} = 0.7$ V, current set point, $I_{\text{set}} = 100$ pA) of MBE-grown epitaxial VSe₂ on HOPG substrate (see [Methods](#) for details). The average thickness of 1.5 VSe₂ layers resulted in monolayer (ML) and bilayer (BL) VSe₂ regions identified within the image. Inset shows the height profile across layers, with the respective step heights indicated. (c,d) Atomically resolved STM topographs (5 × 5 nm², $V_{\text{tip}} = -0.2$ V, $I_{\text{set}} = 200$ pA) of BL (c) and ML (d) VSe₂ at 78 K. Both topographs show a hexagonal lattice with visibly distinct superstructures.

$\lambda_{\text{CDW}} \approx 4a \times 4a \times 3c + \delta$ is commensurate with the in-plane lattice constant a , but incommensurate with the interlayer distance c , and corresponds to a weakly nested FS region, supported by a structured EPC.^{7,20} For thicknesses below 20 nm, the FS of 1T-VSe₂ transitions to 2D character, while maintaining triple-Q, $4a$ CDW order.²¹

Meanwhile, monolayer (ML)-VSe₂, grown epitaxially in several recent works, purportedly hosts a ground state with concomitant charge and spin orders, the nature of which is controversial.^{22–24} First, while some claim $4a$ CDW to be absent even at low temperatures,^{22,24} others indicate its persistence to well above room temperature.²³ Second, several works report incommensurate superstructures with varying periodicities, viz. $\sqrt{3}a \times 2a$, $\sqrt{3}a \times \sqrt{7}a$, and $\sim 2a \times 3a$,^{22–25} whose purported origins vary from structural distortions to nested CDWs. The relation of all these superstructures—identified via electronic density distributions over small real space regions—to any long-ranged charge order remains unclear. Finally, magnetism is suggested to emerge in ML-VSe₂ despite its absence in the bulk,^{22,26} but both its existence and interplay with charge order are actively debated.^{27,28} Disentangling these apparently conflicting observations is paramount to revealing the true nature of charge order in ML-VSe₂, its driving mechanism, and its ramifications on other phases. This requires a controlled and systematic study of the CDW under varying thermodynamic conditions.

Here we report a comprehensive experimental and theoretical investigation of charge order in ultrathin epitaxial 1T-VSe₂. Scanning tunnelling microscopy (STM) experiments show that while the CDW in BL-VSe₂ is closely related to that in bulk, charge order in ML-VSe₂ is qualitatively different. By systematically varying substrates, film thickness, and temperature, we find that ML-VSe₂ consistently hosts two unidirectional (single-Q) CDWs with periods $4a$ and $2.8a$, with strikingly distinct phenomenologies. Band structure calculations elucidate that while the $4a$ CDW is stabilized by conventional FS nesting and EPC, the $2.8a$ CDW cannot be explained by such mechanisms. Instead, we find the $2.8a$

instability to originate from a flat band region, wherein electron–electron interactions are expected to be strongly enhanced. Our results establish ML-VSe₂ as a host of coexisting CDWs with distinct driving mechanisms, demonstrating the potential of correlations for tuning electronic phases in the 2D limit.

RESULTS AND DISCUSSION

STM Imaging Experiments. Thin films of VSe₂ were grown using molecular beam epitaxy (MBE) on highly oriented pyrolytic graphite (HOPG) and MoS₂ substrates under ultrahigh vacuum conditions (see [Methods](#)). Both substrates are known to stabilize the 1T polymorph of VSe₂²² whose crystal structure is shown in [Figure 1a](#). The films were characterized in situ using STM over temperatures of 77–200 K (see [Methods](#)). As shown in [Figure 1b](#), controlled growth of an average thickness of 1.5 layers resulted in the formation of both ML- and BL-VSe₂ regions (on HOPG) within fields-of-view accessible to STM imaging. Topographic characterization of a terraced region at 78 K ([Figure 1b](#): inset) reveals step heights of 0.9 and 0.6 nm for the first and second VSe₂ layers respectively, in line with values reported previously.²³

[Figure 1c,d](#) displays atomic resolution topographs obtained in the BL and ML regions, respectively. As expected, both cases show the expected hexagonal arrangement of atoms with lattice constant, $a \approx 0.34$ nm.^{22,23} Meanwhile, the atomic-scale superstructures seen on ML- and BL-VSe₂ appear starkly different. For BL-VSe₂ ([Figure 1c](#)), the superstructure is tridirectional, that is, it manifests along all three lattice directions with a single length scale. The overall phenomenology is very similar to that of the triple-Q CDW reported in bulk and thinned 1T-VSe₂ crystals.²¹ In contrast, for ML-VSe₂ ([Figure 1d](#)), the superstructure appears unidirectional, and has multiple length scales, consistent with recent results reported by other groups.^{22,23} Crucially, complementary imaging of the ML using noncontact atomic force microscopy under similar conditions shows no corrugations beyond those of the atomic lattice (see [Supporting Information \(SI\) Section S2](#)), which

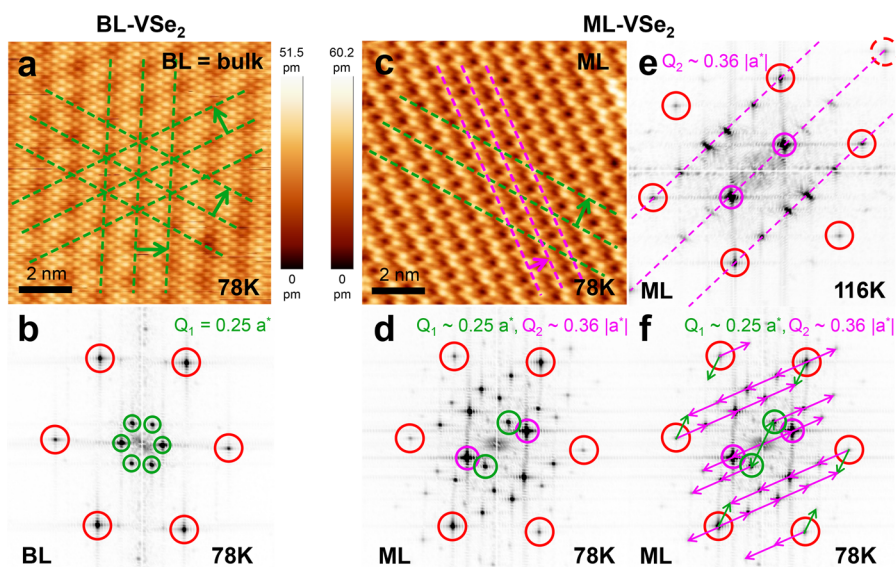


Figure 2. Comparison of CDWs in BL and ML-VSe₂. (a–d) STM topographs (a,c: 10 × 10 nm², $V_{\text{tip}} = -0.2$ V, $I_{\text{tip}} = 200$ pA) and their respective Fourier Transforms (FTs: b,d) acquired at 78 K on BL- (a,b) and ML- (c,d) VSe₂, from adjacent terraces with no observable grain boundary. Dashed color-coded lines in (a,c) represent the real space CDW wavefronts, and corresponding circles in (b,d) denote the respective CDW wavevectors Q_1 (b,d: green) and Q_2 (d: magenta), whose magnitudes are indicated in reciprocal lattice units (rlu). Red circles denote atomic Bragg peaks in all FT images. (e) FT of STM topograph acquired on ML-VSe₂ at 116 K. Magenta circle denotes the Q_2 peak, while the Q_1 peak is absent. Dashed lines indicate the orientation of Q_2 and its harmonics with respect to the Bragg peak (red circle). (f) Annotated FT of ML-VSe₂ at 78 K (cf. data in d). Green (Q_1) and magenta (Q_2) circles identify the primary CDW peaks. Color-coded arrows indicate the positions of harmonics with respect to primary and Bragg peaks. All peaks can be accounted for this way.

rules out structural distortions. Therefore, we conclude that the superstructures observed in STM imaging of ML-VSe₂ must be of electronic origin, and putatively regard them as CDWs.

In light of conflicting reports on the CDW phenomenology in ultrathin VSe₂, we systematically examine in Figure 2 the Fourier space modulations from larger STM topographs obtained for both BL and ML cases. For BL-VSe₂, Figure 2b shows the Fourier transform (FT) of a typical STM topograph. Here we find prominent peaks at $Q_1 \simeq 0.25a^*$ (green circles), where a^* is the magnitude of the reciprocal lattice vector, with C_6 symmetry, that is, along all three Bragg directions. Meanwhile, the anisotropy of Bragg peak intensities may indicate either local uniaxial strain within the sample, or asymmetry in the tip shape. Regardless, these observations are consistent with the triple- Q , $4a$ CDW reported in bulk and thinned $1T - \text{VSe}_2$ crystals.²¹ In contrast, the FT for ML-VSe₂ shown in Figure 2d appears more complex, with only C_2 symmetry present. First, cf. the BL, the ML shows the persistence of the $Q_1 \simeq 0.25a^*$ peak (green circle) along a single Bragg direction, corresponding to a single- Q , $4a$ CDW. Second, the most prominent Fourier peak for the ML is seen at $Q_2 \simeq 0.36a^*$ at an angle $\theta_{12} \sim 30^\circ$ relative to the Bragg direction (magenta circle). As shown in Figure 2f, a careful inspection of the FT for the ML suggests that all remaining Fourier peaks can be assigned to higher harmonics or Bragg reflections of Q_1 and Q_2 , including previously reported multiplet superstructures.^{23–25} While such superstructures may, in principle, be identified with several distinct wavelengths over small topographic regions, such identifications are not consistent over length scales above 5 nm in any of the reported data.^{23–25} Instead, we propose that these apparent supercells are merely the result of superposing two single- Q

CDWs, one of which is aligned away from a high-symmetry direction and also incommensurate with the atomic lattice.

Temperature Dependence. To further establish the character of CDW(s), we studied the evolution of CDW peaks in BL- and ML-VSe₂ with temperature, across both substrates. Notably, the FT of ML-VSe₂ recorded at higher temperatures (Figure 2e) reveal only a single Fourier modulation with magnitude Q_2 , as well as its harmonics and reflections. This further evidence the presence of only two principal CDWs— Q_1 and Q_2 —and suggests that they may have independent origins. At the same time, the slight thermal variation in the direction of Q_2 with respect to the lattice shows that the Q_2 CDW is not strongly coupled to the lattice. It also suggests a potential interplay between the two CDWs, which may lower the energetic cost of the charge ordered state when harmonics and reflections of Q_2 are connected by Q_1 (Figure 2f). Meanwhile, both BL- and ML-VSe₂ grown on MoS₂ substrate (see SI Section S1) exhibit identical CDW phenomenology to their counterparts grown on HOPG (Figure 2), limiting the potential role of substrate-induced strain effects in driving CDW formation.

The thermal evolution of the CDW intensity in STM topographs is an established thermodynamic marker of the CDW transition.^{29,30} In Figure 3, we show representative STM topographs for ML-VSe₂ on HOPG for different temperatures (extended data set in SI Section S3). While the data were recorded over varying fields-of-view, we emphasize that, within our experiments, none of the CDWs exhibit any macroscopic spatial variation across atomically smooth regions. For ease of comparison, the CDW peak intensities plotted in Figure 3 are normalized to the corresponding Bragg peak intensities for each STM topograph. Consistently across BL- and ML-VSe₂, we find that the intensity of Q_1 ($4a$ CDW) drops sharply at ~ 110 K to a negligible magnitude, consistent with the thermal evolution of its bulk counterpart.²¹ The small, finite magnitude

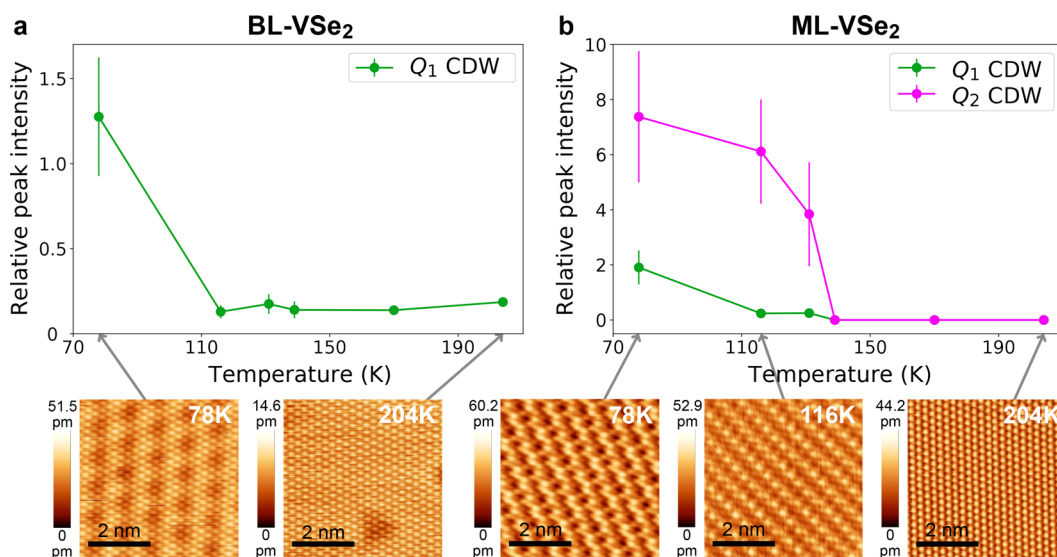


Figure 3. Temperature Dependence of CDW Intensities in ultrathin VSe₂. Thermal evolution of intensities of the CDW peaks, normalized to the averaged intensities of the six primary Bragg peaks at that temperature, as measured from FTs of 10 × 10 nm² STM topographs acquired on (a) BL- and (b) ML-VSe₂, respectively (data set in SI Section S3, Figure S3). Error bars show the standard deviation, incorporating the variance in Bragg and CDW peak intensities at each temperature. Insets show STM topographs at selected temperatures for BL (left) and ML (right), respectively.

of Q_1 in BL-VSe₂ at higher temperatures likely arises from small CDW pockets near defects, similar to defect-pinned CDWs at $T \gg T_{\text{CDW}}$ reported in other TMDCs.^{29,30} Meanwhile, for ML-VSe₂, the intensity of Q_2 —in sharp contrast to Q_1 —remains sizable well above ~110 K, and drops to nearly zero at ~140 K. Finally, no CDW signatures are observed in the 204 K topographs (Figure 3c,g), precluding the persistence of either CDW to room temperature.²³

Overall, our systematic analysis sheds much-needed light on the presence, character, and robustness of putative charge order in ML-VSe₂ in view of conflicting reports in literature.^{23,24,31–33} First, our AFM-STM comparison confirms the purely electronic (CDW) origin of all observed superstructures on ML- and BL-VSe₂ (*cf.* ref 23.). Second, T -dependent experiments conclusively establish the presence of two, and only two, independent single- Q CDWs in ML-VSe₂ — $Q_1 \simeq 0.25a^*$ (*i.e.*, $\lambda_1 \simeq 4a$) and $Q_2 \simeq 0.36a^*$ (*i.e.*, $\lambda_2 \simeq 2.8a$), respectively. The Q_1 CDW is identical in magnitude, orientation, and transition temperature to the triple- Q CDW observed in BL-VSe₂, and to (the in-plane projection of) the CDW reported in bulk crystals. Meanwhile, the Q_2 CDW persists at temperatures well beyond Q_1 and exhibits thermal variations in its orientation with respect to the atomic lattice. Finally, the observed consistency of Q_1 and Q_2 across distinct substrates (*cf.* refs 32 and 33), and of BL-VSe₂ with bulk (*cf.* ref 31), strongly constrain the potential influence of substrate-induced strain effects on the CDW characteristics reported here. To understand the origin of this observed dichotomy in CDW characteristics within the same material, we conduct a detailed examination of the electronic structure of ultrathin VSe₂.

Band Structure Calculations. Density functional theory (DFT) calculations were performed to investigate the atomic and electronic structure of ultrathin 1T-VSe₂ using the Vienna *Ab Initio* Simulation Package (VASP, see Methods).³⁵ ML-VSe₂ was simulated by requiring the interlayer distance to be 25 Å, and relaxing a 4 × 4 atomic supercell structure, both with and without the symmetry constraints of the underlying $P\bar{3}m1$

space group.³⁶ In both cases, the resulting lattice is purely hexagonal, and free of any structural distortions (*cf.* ref 23). This further points to the electronic origin of superstructures observed in ML-VSe₂, in line with our experimental findings. Subsequently, the electronic structure was computed, both with and without including spin polarization. The resulting energies are nearly equal for both cases. This suggests, in conjunction with the absence of spin splitting in angle-resolved photoemission spectroscopy (ARPES) results,^{23,24,26,27,34,37,38} that magnetic order, even if present in ML-VSe₂, is unlikely to play a significant role in the energetics of charge ordered states.

The DFT band structure (Figure 4a) is broadly in agreement with the ARPES spectral function measured for ML-VSe₂.³⁴ The data in ref 34 provides a valuable benchmark given its high quality, large momentum range, and qualitative agreement with other ARPES reports, including data acquired on our samples (SI Section S4, Figure S4).²⁶ Both techniques find a single band of predominantly d -orbital character crossing the Fermi energy E_F . Previous works have emphasized the importance of the nesting of the sides of the FS lobes at the BZ edge.^{23,24,39} The DFT electronic structure, however, underestimates k_F along M–K and suggests a “nesting vector” along a^* of length 0.21 rlu. This falls short of the vector extracted from ARPES data ($0.54 \pm 0.04 \text{ \AA}^{-1}$), which corresponds to 0.25 ± 0.02 rlu.^{27,34} The DFT band along Γ –M also appears more dispersive than that in ARPES, while along Γ –K the DFT band is higher (50–200 meV) than the magnitude expected from the high photoelectron count around Γ .^{23,24,26,27,34,37} These discrepancies are likely due to the inability to duly account for electronic correlations.³⁸ As a result, our *ab initio* calculations may not capture the electronic structure near E_F with sufficient quantitative accuracy to describe CDW energetics.

We therefore complement the DFT calculation with a tight-binding (TB) fit to the ARPES data in ref 34 (see Methods), the results of which are compared to the DFT in Figure 4. In agreement with reported ARPES spectra, the TB fit shows a flat band region around the Γ -point, an indicator of strong

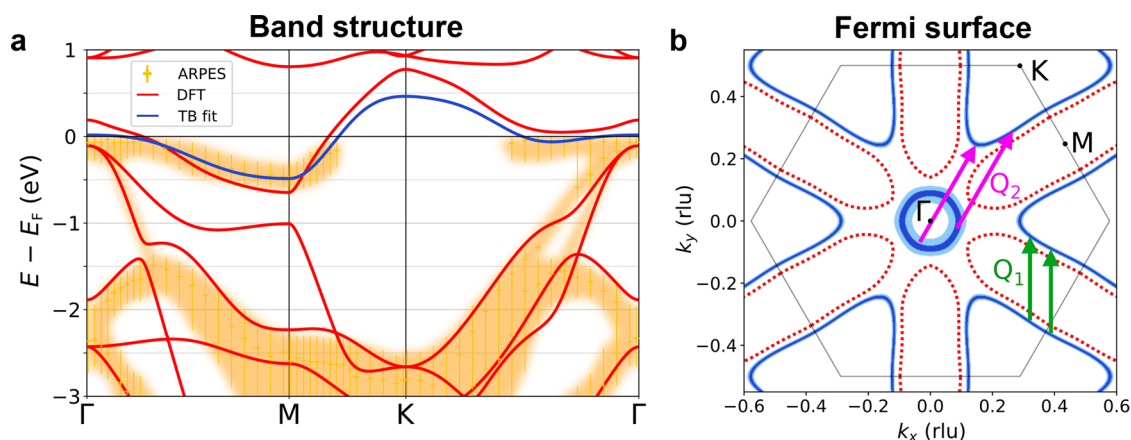


Figure 4. Electronic Structure of ML-VSe₂. (a) Electronic band structure of ML-VSe₂ obtained from DFT calculations (red line), compared to published ARPES measurements of the spectral function for epitaxially grown ML-VSe₂ at $T = 170$ K (shaded yellow, crosses: peak positions, lines: full width at half-maximum). The line width of the experimental data greatly exceeds the experimental resolution.³⁴ Blue line is a tight-binding (TB) fit to the ARPES-measured, near- E_F band structure, where E_F is the Fermi energy. (b) Fermi surface (FS) of ML-VSe₂, obtained from the TB fit in (a) by plotting states within ± 1 meV (dark blue) and ± 10 meV ($\approx k_B T$ for $T = 100$ K, light blue) of E_F . Dotted red line shows the DFT FS, which qualitatively deviates from the TB fit. Hexagon shows the Brillouin zone (BZ), and the arrows indicate FS regions visually appearing to be nested by the experimentally determined CDW wavevectors.

correlations. The difference in topology between the DFT and TB FS (Figure 4b) is due to the proximity of a van Hove singularity to E_F .³⁴ Overlaying the CDW vectors extracted from our STM data onto the FS visually suggests that Q_1 corresponds to nesting between the sides of neighboring triangular FS pockets at the BZ edge, while Q_2 connects the flat-band region around Γ to the pocket corners around K.

Nesting and Correlated Instabilities. A conventional CDW instability at wavevector \mathbf{Q}_{CDW} results from a maximum in its electronic susceptibility $D_2(\mathbf{q})$ for $\mathbf{q} = \mathbf{Q}_{\text{CDW}}$.^{2,40} In the weak electron–phonon coupling (EPC) limit (see Methods), $D_2(\mathbf{q})$ can be expressed as⁴⁰

$$D_2(\mathbf{q}) = - \sum_{\mathbf{k} \in \text{BZ}} |g_{\mathbf{k}, \mathbf{k}+\mathbf{q}}|^2 \frac{f(E_{\mathbf{k}}) - f(E_{\mathbf{k}+\mathbf{q}})}{E_{\mathbf{k}} - E_{\mathbf{k}+\mathbf{q}} + i\delta} \quad (1)$$

Here, $f(E)$ is the Fermi–Dirac function, $E_{\mathbf{k}}$ is the bare (nonrenormalized) electronic dispersion, and δ is a small regulator (0.1 meV in this work). The EPC matrix elements, $|g_{\mathbf{k}, \mathbf{k}+\mathbf{q}}|$, are often approximated to unity, resulting in the Lindhard, or bare susceptibility, $\chi(\mathbf{q})$. However, for TMDCs whose near- E_F behavior is governed by d -band(s), several works have established a more realistic approximation to $|g_{\mathbf{k}, \mathbf{k}+\mathbf{q}}|$ via the electronic band structure^{7,41,42} (see Methods). Here, we use the TB fit to calculate the bare ($\chi(\mathbf{q})$) and structured ($D_2(\mathbf{q})$) electronic susceptibilities, which are shown in Figure 5a,b, respectively.

The green circles in Figure 5a,b indicates the maximum of the bare (structured) susceptibility, which lies at $\mathbf{Q} = (0, 0.28) \approx \mathbf{Q}_1$. Its proximity to a commensurate value suggests that the corresponding CDW will lock to 0.25 rlu ($\lambda = 4a$) due to CDW–lattice interactions.⁴ Although its periodicity is the same as that of the CDW observed in bulk and BL-VSe₂, the FS for the ML is strictly 2D, and the parts of the FS involved in CDW formation may be different. To elucidate the role of the FS in the observed CDWs, we plot in Figure 5c,d the \mathbf{k} -resolved contributions to $\chi(\mathbf{q})$ and $D_2(\mathbf{q})$ for $\mathbf{q} = \mathbf{Q}_1$. As anticipated in Figure 4b, the dominant contributions to $\chi(\mathbf{Q}_1)$ arise from the parallel edges of the K-centered pockets, while the Γ -centered FS region plays a negligible role. The well-nested K-pocket

edges with opposite group velocities are therefore inherently unstable to a Peierls-like CDW. The EPC matrix elements further enhance the contribution of these \mathbf{Q}_1 -connected regions to $D_2(\mathbf{Q}_1)$, thereby confirming the conventional origin of the \mathbf{Q}_1 CDW in ML-VSe₂.

In contrast, the phenomenology for $\mathbf{q} = \mathbf{Q}_2$ does not fit the conventional CDW framework. As highlighted by the magenta circles in Figure 5a,b, this wavevector lies in the middle of a susceptibility plateau, and lacks a well-defined maximum. The dominant contribution to the bare susceptibility at $\mathbf{q} = \mathbf{Q}_2$ comes from the Γ -centered flat band region, with smaller contributions from the K-centered pockets (see Figure 5e). However, the corresponding $D_2(\mathbf{k}, \mathbf{Q}_2)$ in Figure 5f shows that the EPC matrix elements strongly suppress the intensity in these regions, and the remaining contributions are insufficient to drive the \mathbf{Q}_2 CDW according to an EPC-assisted Peierls scenario. While the perturbative expansion used for the structured susceptibility calculations^{7,40–42} may not fully capture EPC in flat bands, that the origin of the \mathbf{Q}_2 CDW lies beyond the Peierls description of CDWs is consistent with its empirical characteristics, viz. varying orientation with respect to the lattice, absence in BLs (and beyond), and the lack of a discernible peak in $\chi(\mathbf{q})$.

In the 2D limit of layered TMDCs like 1T-VSe₂, the screening of Coulomb interactions between electrons is much reduced.⁴³ The relative importance of the unscreened interactions is further enhanced within flat bands associated with a van Hove singularity, such as at the near- Γ region in ML-VSe₂ (Figure 4).^{23,34,37,38} Indeed, the measured line width, or self-energy, of the band near E_F is much larger than the experimental resolution,³⁴ supporting the presence of strong electronic correlations.⁴⁴ Such interactions can considerably renormalize electron and phonon properties, and enable CDW order at momenta that do not correspond to peaks in the conventional susceptibility ($\chi(\mathbf{q})$ or $D_2(\mathbf{q})$). Indeed, such correlation-driven CDWs have been predicted to exist in TMDCs,⁸ including in ML-VSe₂,³⁹ and are consistent with the unusual characteristics of the \mathbf{Q}_2 CDW. Crucially, a correlation-driven mechanism for the \mathbf{Q}_2 CDW offers the only viable explanation of its prevalence over a well-nested

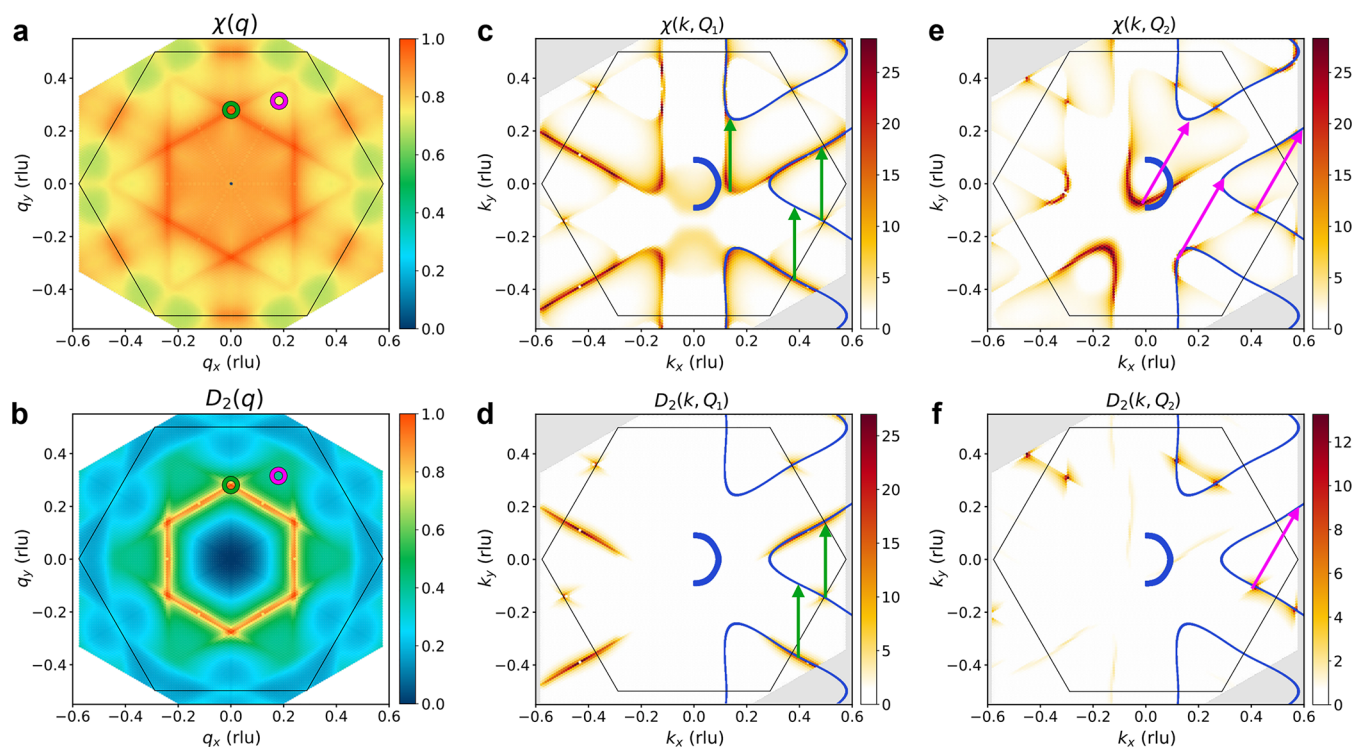


Figure 5. Momentum Space Diagnostics of ML-VSe₂ CDWs. (a) The normalized Lindhard susceptibility χ and (b) structured electronic susceptibility D_2 derived from the TB band structure. Circles highlight the positions of the susceptibility maximum $(0, 0.28) \approx Q_1$ (green) and experimentally determined $Q_2 = (0.182, 0.315)$ (magenta), with the latter being located on an intensity plateau. (c–f) Diagnostics indicating the BZ regions contributing to the two susceptibilities χ and D_2 , given a chosen wavevector Q_1 (c,d) or Q_2 (e,f). Blue lines denote FS contours in the right half of the images, while black hexagons indicate the BZ. Q_1 (green) and Q_2 (magenta) arrows indicate the regions with prominent contributions to the susceptibilities as deduced from the diagnostics.

counterpart (Q_1), and the complete gapping of the FS,^{23,34,37,38} despite the absence of any associated feature in susceptibility calculations based on models of noninteracting electrons. Further, we conjecture that the single- q character of the Q_2 CDW, which breaks the 3-fold rotational symmetry of the lattice, makes it energetically favorable for the Q_1 CDW (nominally triple- q) to also order in a single- q configuration. The interplay of these CDWs could be examined in future theoretical works by iteratively incorporating the resulting lattice distortions.

CONCLUSIONS

In summary, our systematic experimental and theoretical efforts elucidate that 1T-VSe₂ undergoes a dimensional crossover as its thickness is reduced to a single layer. While BL-VSe₂, akin to bulk, hosts a conventional triple- Q CDW, ML-VSe₂ hosts two distinct single- Q CDWs with contrasting characteristics. One, with $\lambda_1 \approx 4a$, behaves similarly to its BL/bulk counterpart, and arises from a weak-coupling Peierls mechanism utilizing nested FS regions. In contrast, the dominant CDW, with $\lambda_2 \approx 2.8a$, cannot be explained within the conventional EPC-assisted Peierls framework. Instead, the observed thermal evolution and the calculated susceptibility suggest that this CDW—unique to the ML—arises from a flat region of the electronic band structure, where interactions and correlation effects are expected to dominate.

Monolayer VSe₂ stands apart in hosting two coexisting charge orders with distinct physical origins. Conventional electronic materials are typecast by the mechanisms and phenomena they host. Our work suggests that ML-VSe₂

transcends such labeling, and hosts coexisting ordered states originating from contrasting coupling mechanisms. The prospect of such emergent electron correlations and ensuing ordered states presenting themselves in 2D TMDCs more generally is particularly promising given their predominance in the plethora of proposed designs for heterogeneous layered materials.^{10,45,46} Their potential for tunability and their interplay with conventional charge and spin orders in the ultrathin limit is promising for realizing exotic ordered states on one the hand, and for applications in multifunctional electronics on the other.

METHODS

Film Growth. 1T-VSe₂ films were grown on HOPG substrates in a homemade, ultrahigh-vacuum molecular beam epitaxy (MBE) system, the growth chamber of which has a base pressure of 2×10^{-9} mbar. The substrate was exfoliated *ex situ*, immediately transferred into the MBE chamber, and then outgassed at 420 °C for 3 h before MBE growth. The VSe₂ samples were grown via simultaneously evaporating V and Se using an electron-beam evaporator and a Knudsen cell, respectively, onto the substrates maintained at 360 °C. The Se/V ratio was high, and Se was controlled to be in excess. A selenium capping layer was deposited onto the VSe₂ surface to prevent direct ambient contamination during *ex situ* transport to the varying temperature STM/nc-AFM system for subsequent measurements. The capping layer was removed by annealing at 240 °C for 30 min in the microscope chamber.

STM and AFM Measurements. STM/nc-AFM measurements were performed over 78–204 K in an Omicron UHV system interfaced to a Nanonis controller equipped with STM/qPlus sensor and an electrical local heater. To reduce thermal drift during data acquisition, the STM was first allowed to stabilize at each

temperature. Electrochemically etched tungsten tips were used with bias voltage applied to the tip, while the sample holder was grounded. STM images were acquired using constant current mode. For nc-AFM imaging, the constant-height mode with an oscillation amplitude of 10 nm was used to record the frequency shift (Δf) of the qPlus resonator (sensor frequency $f_0 \approx 24$ kHz, $Q \approx 8000$). A lock-in technique was used to measure dI/dV spectra, with a modulation of 625 Hz and 30 mV.

DFT Calculations. 1T-VSe₂ belongs to the space group $P\bar{3}m1$, with the lattice parameters for the monolayer crystal being $a = b = 3.33$ Å, $\gamma = 120^\circ$.³⁶ First-principle atomic and electronic structure calculations were performed within the density functional theory (DFT) framework as implemented in the Vienna *Ab Initio* Simulation Package (VASP)³⁵ with a plane-wave basis up to a cutoff of 500 eV. To simulate the monolayer, we artificially set the distance between two layers of VSe₂ to 25 Å. The Perdew–Burke–Ernzerhof (PBE)⁴⁷ form was used for the exchange–correlation functional. The Γ -centered k -mesh was set to be $25 \times 25 \times 1$ in the Brillouin zone for the self-consistent calculation. The relaxation of atomic structure was done in two ways. First, a 4×4 supercell was relaxed under the symmetry constraints of the space group. This process was then repeated without any symmetry constraints applied.

Tight-Binding Calculations. A tight-binding fit was performed for the single d -orbital band crossing the Fermi level in the available ARPES data of ref 34. To obtain the best fit, we used an expansion of the dispersion $E(\mathbf{k})$ in functions respecting the lattice symmetries. Including terms to fifth order, the fit can be expressed as

$$E(\mathbf{k}) = t_0 + t_1(2 \cos(\xi)\cos(\eta) + \cos(2\xi)) + t_2(2 \cos(3\xi)\cos(\eta) + \cos(2\eta)) + t_3(2 \cos(2\xi)\cos(2\eta) + \cos(4\xi)) + t_4(\cos(\xi)\cos(3\eta) + \cos(5\xi)\cos(\eta) + \cos(4\xi)\cos(2\eta)) + t_5(2 \cos(3\xi)\cos(3\eta) + \cos(6\xi)) \quad (2)$$

where $\xi = \frac{1}{2}k_x$ and $\eta = \frac{\sqrt{3}}{2}k_y$, while k_x, k_y are given in units of $\frac{2\pi}{a}$, with a the lattice parameter. t_i are the (in-plane) hopping amplitudes. The best fit to ARPES data based on this form of the dispersion is shown in Figure 4.

Susceptibility Calculations. In the limit of weak electron–phonon coupling, the electronic susceptibility can be derived from a perturbative expansion of the phonon propagator, using the random phase approximation (RPA). Neglecting vertex corrections, which should be small,⁴⁸ the renormalized phonon propagator is described by $D_{\text{RPA}} = (D_0^{-1} - D_2)^{-1}$, with bare phonon propagator D_0 and electronic susceptibility D_2 , given by^{5,7,40}

$$D_2(\mathbf{q}) = - \sum_{\mathbf{k} \in \text{BZ}} |g_{\mathbf{k}, \mathbf{k}+\mathbf{q}}|^2 \frac{f(E_{\mathbf{k}}) - f(E_{\mathbf{k}+\mathbf{q}})}{E_{\mathbf{k}} - E_{\mathbf{k}+\mathbf{q}} + i\delta} \quad (3)$$

Here, $f(E)$ is the Fermi–Dirac distribution function, $E_{\mathbf{k}}$ is the nonrenormalized electronic dispersion and we use a small regulator $\delta = 0.1$ meV. If the system has an intrinsic or electron–phonon driven CDW instability within the weak-coupling limit, the susceptibility will exhibit a maximum at the CDW wave vector \mathbf{Q} . Generally, the electron–phonon coupling (EPC) matrix elements $|g_{\mathbf{k}, \mathbf{k}+\mathbf{q}}|^2$ are difficult to compute exactly. For this reason, it is common to set them to unity, resulting in the Lindhard function:

$$\chi(\mathbf{q}) = - \sum_{\mathbf{k} \in \text{BZ}} \frac{f(E_{\mathbf{k}}) - f(E_{\mathbf{k}+\mathbf{q}})}{E_{\mathbf{k}} - E_{\mathbf{k}+\mathbf{q}} + i\delta} \quad (4)$$

In previous works, it has been shown that the EPC matrix elements can be approximated based purely on the electronic dispersion. This approximation has been well-tested for transition metal compounds with d -orbital character at E_F .^{7,41,42} In the case of a single band crossing E_F , the expression becomes

$$\mathbf{g}_{\mathbf{k}, \mathbf{k}+\mathbf{q}} \propto \frac{\partial E_{\mathbf{k}}}{\partial \mathbf{k}} - \frac{\partial E_{\mathbf{k}+\mathbf{q}}}{\partial \mathbf{k}} \quad (5)$$

The orientation of $\mathbf{g}_{\mathbf{k}, \mathbf{k}+\mathbf{q}}$ indicates the direction of phonon polarization. We consider longitudinal CDWs, such that the relevant component of the EPC vector is parallel to the in-plane phonon momentum: $g_{\mathbf{k}, \mathbf{k}+\mathbf{q}} = \mathbf{g}_{\mathbf{k}, \mathbf{k}+\mathbf{q}} \cdot \mathbf{q}_{\parallel} / |\mathbf{q}_{\parallel}|$.

ASSOCIATED CONTENT

Supporting Information

The Supporting Information is available free of charge at <https://pubs.acs.org/doi/10.1021/acsnano.1c08304>.

Supporting data on MoS₂ substrate; comparison of STM- and AFM-imaging of ML-VSe₂; full data set for temperature-dependence presented in manuscript; and comparison of tight-binding fit to ARPES data (PDF)

AUTHOR INFORMATION

Corresponding Authors

Jasper van Wezel – *Institute for Theoretical Physics Amsterdam and Delta Institute for Theoretical Physics, University of Amsterdam, Amsterdam 1098XH, The Netherlands*; Email: j.vanwezel@uva.nl

Anjan Soumyanarayanan – *Department of Physics, National University of Singapore, Singapore 117542, Singapore; Institute of Materials Research & Engineering (IMRE), Agency for Science, Technology and Research (A*STAR), Singapore 138634, Singapore*; orcid.org/0000-0003-2680-6005; Email: anjan@nus.edu.sg

Andrew T. S. Wee – *Department of Physics, National University of Singapore, Singapore 117542, Singapore*; orcid.org/0000-0002-5828-4312; Email: phyweets@nus.edu.sg

Authors

Rebekah Chua – *Department of Physics, National University of Singapore, Singapore 117542, Singapore*

Jans Henke – *Institute for Theoretical Physics Amsterdam and Delta Institute for Theoretical Physics, University of Amsterdam, Amsterdam 1098XH, The Netherlands*

Surabhi Saha – *Department of Physics, Indian Institute of Science, Bangalore 560012, India*

Yuli Huang – *Department of Physics, National University of Singapore, Singapore 117542, Singapore; Joint School of National University of Singapore and Tianjin University, Fuzhou 350207, China*; orcid.org/0000-0003-3699-4708

Jian Gou – *Department of Physics, National University of Singapore, Singapore 117542, Singapore*

Xiaoyue He – *Department of Physics, National University of Singapore, Singapore 117542, Singapore; Songshan Lake Materials Laboratory, Dongguan, Guangdong 523808, China*

Tanmoy Das – *Department of Physics, Indian Institute of Science, Bangalore 560012, India*

Complete contact information is available at: <https://pubs.acs.org/doi/10.1021/acsnano.1c08304>

Author Contributions

[†]R.C. and J.H. contributed equally to this work.

Author Contributions

R.C., Y.L.H., J.G., and X.H. performed the experiments and analyzed the data. S.S. and T.D. performed the *ab initio*

calculations. J.H. performed the tight-binding and susceptibility calculations. J.v.W., A.S., and A.T.S.W. coordinated and supervised the work. All authors discussed the results and provided inputs to the manuscript.

Notes

The authors declare no competing financial interest.

ACKNOWLEDGMENTS

The work in Singapore was funded by the Ministry of Education Tier 2 grant no. MOE2017-T2-2-139. J.G. acknowledges funding from NRF-NSFC under grant no. R-144-000-405-281, and A.S. acknowledges the support of A*STAR Singapore under the SpOT-LITE programme (Grant no. A18A6b0057). T.D. acknowledges the support of the Department of Science, Government of India under the project R(RO)/DST/NSM/HPC_Applications/2021-1464. The computational work at IISc also benefited from the S.E.R.C. supercomputing facility.

REFERENCES

- (1) Grüner, G. The Dynamics of Charge-Density Waves. *Rev. Mod. Phys.* **1988**, *60*, 1129–1181.
- (2) Johannes, M. D.; Mazin, I. I. Fermi Surface Nesting and the Origin of Charge Density Waves in Metals. *Phys. Rev. B: Condens. Matter Mater. Phys.* **2008**, *77*, 165135.
- (3) Zhu, X.; Cao, Y.; Zhang, J.; Plummer, E. W.; Guo, J. Classification of Charge Density Waves Based on Their Nature. *Proc. Natl. Acad. Sci. U. S. A.* **2015**, *112*, 2367–2371.
- (4) Feng, Y.; van Wezel, J.; Wang, J.; Flicker, F.; Silevitch, D. M.; Littlewood, P. B.; Rosenbaum, T. F. Itinerant Density Wave Instabilities at Classical and Quantum Critical Points. *Nat. Phys.* **2015**, *11*, 865–871.
- (5) Flicker, F.; van Wezel, J. Charge Order from Orbital-Dependent Coupling Evidenced by NbSe₂. *Nat. Commun.* **2015**, *6*, 7034.
- (6) Kogar, A.; Rak, M. S.; Vig, S.; Husain, A. A.; Flicker, F.; Joe, Y. I.; Venema, L.; MacDougall, G. J.; Chiang, T. C.; Fradkin, E.; van Wezel, J.; Abbamonte, P. Signatures of Exciton Condensation in a Transition Metal Dichalcogenide. *Science* **2017**, *358*, 1314–1317.
- (7) Henke, J.; Flicker, F.; Laverock, J.; van Wezel, J. Charge Order from Structured Coupling in VSe₂. *SciPost Physics* **2020**, *9*, 56.
- (8) Chen, C.-W.; Choe, J.; Morosan, E. Charge Density Waves in Strongly Correlated Electron Systems. *Rep. Prog. Phys.* **2016**, *79*, No. 084505.
- (9) Steinke, C.; Wehling, T. O.; Rösner, M. Coulomb-Engineered Heterojunctions and Dynamical Screening in Transition Metal Dichalcogenide Monolayers. *Phys. Rev. B: Condens. Matter Mater. Phys.* **2020**, *102*, 115111.
- (10) Novoselov, K. S.; Jiang, D.; Schedin, F.; Booth, T. J.; Khotkevich, V. V.; Morozov, S. V.; Geim, A. K. Two-Dimensional Atomic Crystals. *Proc. Natl. Acad. Sci. U. S. A.* **2005**, *102*, 10451–3.
- (11) Li, L. J.; O'Farrell, E. C. T.; Loh, K. P.; Eda, G.; Özyilmaz, B.; Castro Neto, A. H. Controlling Many-Body States by the Electric-Field Effect in a Two-Dimensional Material. *Nature* **2016**, *529*, 185–189.
- (12) Tsen, A. W.; Hovden, R.; Wang, D.; Kim, Y. D.; Okamoto, J.; Spoth, K. A.; Liu, Y.; Lu, W.; Sun, Y.; Hone, J. C.; Kourkoutis, L. F.; Kim, P.; Pasupathy, A. N. Structure and Control of Charge Density Waves in Two-Dimensional 1T-TaS₂. *Proc. Natl. Acad. Sci. U. S. A.* **2015**, *112*, 15054–15059.
- (13) Gao, S.; Flicker, F.; Sankar, R.; Zhao, H.; Ren, Z.; Rachmilowitz, B.; Balachandrar, S.; Chou, F.; Burch, K. S.; Wang, Z.; van Wezel, J.; Zeljkovic, I. Atomic-Scale Strain Manipulation of a Charge Density Wave. *Proc. Natl. Acad. Sci. U. S. A.* **2018**, *115*, 6986–6990.
- (14) Abram, M.; Zegrodnik, M.; Spalek, J. Antiferromagnetism, Charge Density Wave, and d-Wave Superconductivity in the Extended tJU Model: Role of Intersite Coulomb Interaction and a Critical Overview of Renormalized Mean Field Theory. *J. Phys.: Condens. Matter* **2017**, *29*, 365602.
- (15) Butler, C. J.; Yoshida, M.; Hanaguri, T.; Iwasa, Y. Doublylonlike Excitations and Their Phononic Coupling in a Mott Charge-Density-Wave System. *Phys. Rev. X* **2021**, *11*, No. 011059.
- (16) Lopes, N.; Reyes, D.; Continentino, M. A.; Thomas, C. Interplay between Charge Density Wave and Superconductivity in Multi-Band Systems with Inter-Band Coulomb Interaction. *Phys. Rev. B: Condens. Matter Mater. Phys.* **2021**, *103*, 195150.
- (17) Rossnagel, K. On the Origin of Charge-Density Waves in Select Layered Transition-Metal Dichalcogenides. *J. Phys.: Condens. Matter* **2011**, *23*, 213001.
- (18) Xi, X.; Zhao, L.; Wang, Z.; Berger, H.; Forró, L.; Shan, J.; Mak, K. F. Strongly Enhanced Charge-Density-Wave Order in Monolayer NbSe₂. *Nat. Nanotechnol.* **2015**, *10*, 765–769.
- (19) Barja, S.; Wickenburg, S.; Liu, Z. F.; Zhang, Y.; Ryu, H.; Ugeda, M. M.; Hussain, Z.; Shen, Z.-X.; Mo, S. K.; Wong, E.; Salmeron, M. B.; Wang, F.; Crommie, M. F.; Ogleter, D. F.; Neaton, J. B.; Weber-Bargioni, A. Charge Density Wave Order in 1D Mirror Twin Boundaries of Single-Layer MoSe₂. *Nat. Phys.* **2016**, *12*, 751–756.
- (20) Strocov, V. N.; Shi, M.; Kobayashi, M.; Monney, C.; Wang, X.; Krempasky, J.; Schmitt, T.; Patthey, L.; Berger, H.; Blaha, P. Three-Dimensional Electron Realm in VSe₂ by Soft-X-Ray Photoelectron Spectroscopy: Origin of Charge-Density Waves. *Phys. Rev. Lett.* **2012**, *109*, No. 086401.
- (21) Pásztor, A.; Scarfato, A.; Barreteau, C.; Giannini, E.; Renner, C. Dimensional Crossover of the Charge Density Wave Transition in Thin Exfoliated VSe₂. *2D Mater.* **2017**, *4*, No. 041005.
- (22) Bonilla, M.; Kolekar, S.; Ma, Y.; Diaz, H. C.; Kalappattil, V.; Das, R.; Eggers, T.; Gutierrez, H. R.; Phan, M.-H.; Batzill, M. Strong Room-Temperature Ferromagnetism in VSe₂ Monolayers on van der Waals Substrates. *Nat. Nanotechnol.* **2018**, *13*, 289–293.
- (23) Duvjir, G.; Choi, B. K.; Jang, I.; Ulstrup, S.; Kang, S.; Thi Ly, T.; Kim, S.; Choi, Y. H.; Jozwiak, C.; Bostwick, A.; Rotenberg, E.; Park, J.-G.; Sankar, R.; Kim, K.-S.; Kim, J.; Chang, Y. J. Emergence of a Metal–Insulator Transition and High-Temperature Charge-Density Waves in VSe₂ at the Monolayer Limit. *Nano Lett.* **2018**, *18*, 5432–5438.
- (24) Chen, P.; Pai, W. W.; Chan, Y.-H.; Madhavan, V.; Chou, M. Y.; Mo, S.-K.; Fedorov, A.-V.; Chiang, T.-C. Unique Gap Structure and Symmetry of the Charge Density Wave in Single-Layer VSe₂. *Phys. Rev. Lett.* **2018**, *121*, 196402.
- (25) Ly, T. T.; Duvjir, G.; Lam, N. H.; Kim, J.; Choi, B. K.; Chang, Y. J. $\sqrt{3} \times 2$ and $\sqrt{3} \times \sqrt{7}$ Charge Density Wave Driven by Lattice Distortion in Monolayer VSe₂. *J. Korean Phys. Soc.* **2020**, *76*, 412–415.
- (26) Wong, P. K. J.; Zhang, W.; Bussolotti, F.; Yin, X.; Heng, T. S.; Zhang, L.; Huang, Y. L.; Vinai, G.; Krishnamurthi, S.; Bukhvalov, D. W.; Zheng, Y. J.; Chua, R.; N'Diaye, A. T.; Morton, S. A.; Yang, C.-Y.; Ou Yang, K.-H.; Torelli, P.; Chen, W.; Goh, K. E. J.; Ding, J.; et al. Evidence of Spin Frustration in a Vanadium Diselenide Monolayer Magnet. *Adv. Mater.* **2019**, *31*, 1901185.
- (27) Coelho, P. M.; Nguyen Cong, K.; Bonilla, M.; Kolekar, S.; Phan, M.-H.; Avila, J.; Asensio, M. C.; Oleynik, I. I.; Batzill, M. Charge Density Wave State Suppresses Ferromagnetic Ordering in VSe₂ Monolayers. *J. Phys. Chem. C* **2019**, *123*, 14089–14096.
- (28) Chua, R.; Yang, J.; He, X.; Yu, X.; Yu, W.; Bussolotti, F.; Wong, P. K. J.; Loh, K. P.; Breese, M. B. H.; Goh, K. E. J.; Huang, Y. L.; Wee, A. T. S. Can Reconstructed Se-Deficient Line Defects in Monolayer VSe₂ Induce Magnetism? *Adv. Mater.* **2020**, *32*, 2000693.
- (29) Arguello, C. J.; Chockalingam, S. P.; Rosenthal, E. P.; Zhao, L.; Gutiérrez, C.; Kang, J. H.; Chung, W. C.; Fernandes, R. M.; Jia, S.; Millis, A. J.; Cava, R. J.; Pasupathy, A. N. Visualizing the Charge Density Wave Transition in 2H-NbSe₂ in Real Space. *Phys. Rev. B: Condens. Matter Mater. Phys.* **2014**, *89*, 235115.
- (30) Chatterjee, U.; Zhao, J.; Iavarone, M.; Capua, R. D.; Castellan, J. P.; Karapetrov, G.; Malliakas, C. D.; Kanatzidis, M. G.; Claus, H.; Ruff, J. P. C.; Weber, F.; Wezel, J. v.; Campuzano, J. C.; Osborn, R.; Randeria, M.; Trivedi, N.; Norman, M. R.; Rosenkranz, S. Emergence

of Coherence in the Charge-Density Wave State of $2H\text{-NbSe}_2$. *Nat. Commun.* **2015**, *6*, 6313.

(31) Zhang, D.; Ha, J.; Baek, H.; Chan, Y. H.; Natterer, F. D.; Myers, A. F.; Schumacher, J. D.; Cullen, W. G.; Davydov, A. V.; Kuk, Y.; Chou, M. Y.; Zhitenev, N. B.; Strosio, J. A. Strain engineering a $4a \times \sqrt{3}a$ charge-density-wave phase in transition-metal dichalcogenide $1T\text{-VSe}_2$. *Phys. Rev. Materials* **2017**, *1*, 024005.

(32) Chen, G.; Howard, S. T.; Maghirang, A. B.; Nguyen Cong, K.; Villaos, R. A. B.; Feng, L.-Y.; Cai, K.; Ganguli, S. C.; Swiech, W.; Morosan, E.; Oleynik, I. I.; Chuang, F.-C.; Lin, H.; Madhavan, V. Correlating Structural, Electronic, and Magnetic Properties of Epitaxial VSe_2 Thin Films. *Phys. Rev. B: Condens. Matter Mater. Phys.* **2020**, *102*, 115149.

(33) Duvjir, G.; Choi, B. K.; Ly, T. T.; Lam, N. H.; Jang, K.; Dung, D. D.; Chang, Y. J.; Kim, J. Multiple Charge Density Wave Phases of Monolayer VSe_2 Manifested by Graphene Substrates. *Nanotechnology* **2021**, *32*, 364002.

(34) Feng, J.; Biswas, D.; Rajan, A.; Watson, M. D.; Mazzola, F.; Clark, O. J.; Underwood, K.; Marković, I.; McLaren, M.; Hunter, A.; Burn, D. M.; Duffy, L. B.; Barua, S.; Balakrishnan, G.; Bertran, F.; Le Févre, P.; Kim, T. K.; van der Laan, G.; Hesjedal, T.; Wahl, P.; et al. Electronic Structure and Enhanced Charge-Density Wave Order of Monolayer VSe_2 . *Nano Lett.* **2018**, *18*, 4493–4499.

(35) Kresse, G.; Furthmüller, J. Efficient Iterative Schemes for *ab Initio* Total-Energy Calculations Using a Plane-Wave Basis Set. *Phys. Rev. B: Condens. Matter Mater. Phys.* **1996**, *54*, 11169–11186.

(36) Li, F.; Tu, K.; Chen, Z. Versatile Electronic Properties of VSe_2 Bulk, Few-Layers, Monolayer, Nanoribbons, and Nanotubes: A Computational Exploration. *J. Phys. Chem. C* **2014**, *118*, 21264–21274.

(37) Umemoto, Y.; Sugawara, K.; Nakata, Y.; Takahashi, T.; Sato, T. Pseudogap, Fermi Arc, and Peierls-Insulating Phase Induced by 3D–2D Crossover in Monolayer VSe_2 . *Nano Res.* **2019**, *12*, 165–169.

(38) Biswas, D.; Jones, A. J. H.; Majchrzak, P.; Choi, B. K.; Lee, T.-H.; Volckaert, K.; Feng, J.; Marković, I.; Andreatta, F.; Kang, C.-J.; Kim, H. J.; Lee, I. H.; Jozwiak, C.; Rotenberg, E.; Bostwick, A.; Sanders, C. E.; Zhang, Y.; Karras, G.; Chapman, R. T.; Wyatt, A. S.; et al. Ultrafast Triggering of Insulator-Metal Transition in Two-Dimensional VSe_2 . *Nano Lett.* **2021**, *21*, 1968–1975.

(39) Trott, M. J.; Hooley, C. A. Can Fermi Surface Nesting Alone Drive the Charge-Density-Wave Transition in Monolayer Vanadium Diselenide? **2020**, 2004.06665. *arXiv e-prints*. <https://arxiv.org/abs/2004.06665> (accessed 2021/12/5).

(40) Doran, N. J. A Calculation of the Electronic Response Function in $2H\text{-NbSe}_2$ Including Electron-Phonon Matrix Element Effects. *J. Phys. C: Solid State Phys.* **1978**, *11*, L959–L962.

(41) Varma, C. M.; Blount, E. I.; Vashishta, P.; Weber, W. Electron-Phonon Interactions in Transition Metals. *Phys. Rev. B: Condens. Matter Mater. Phys.* **1979**, *19*, 6130.

(42) Flicker, F.; van Wezel, J. Charge Order in NbSe_2 . *Phys. Rev. B: Condens. Matter Mater. Phys.* **2016**, *94*, 235135.

(43) Nozieres, P. *Theory Of Interacting Fermi Systems*; Westview Press: New York, 1964.

(44) Damascelli, A.; Hussain, Z.; Shen, Z.-X. Angle-Resolved Photoemission Studies of the Cuprate Superconductors. *Rev. Mod. Phys.* **2003**, *75*, 473–541.

(45) Geim, A. K.; Grigorieva, I. V. van der Waals Heterostructures. *Nature* **2013**, *499*, 419–425.

(46) Novoselov, K. S.; Mishchenko, A.; Carvalho, A.; Castro Neto, A. H. 2D Materials and van der Waals Heterostructures. *Science* **2016**, *353*, aac9439.

(47) Perdew, J. P.; Burke, K.; Ernzerhof, M. Generalized Gradient Approximation Made Simple. *Phys. Rev. Lett.* **1996**, *77*, 3865–3868.

(48) Migdal, A. Interaction between Electrons and Lattice Vibrations in a Normal Metal. *Soviet Physics JETP* **1958**, *7*, 996–1001.

Recommended by ACS

Out-of-Plane Transport of $1T\text{-TaS}_2$ /Graphene-Based van der Waals Heterostructures

Carla Boix-Constant, Eugenio Coronado, *et al.*

JULY 06, 2021
ACS NANO

READ 

Observation of Single-Electron Transport and Charging on Individual Point Defects in Atomically Thin WSe_2

Rui Zhang, Jeffrey R. Guest, *et al.*

JUNE 17, 2021
THE JOURNAL OF PHYSICAL CHEMISTRY C

READ 

Charge Density Modulation and the Luttinger Liquid State in MoSe_2 Mirror Twin Boundaries

Yipu Xia, Maohai Xie, *et al.*

AUGUST 06, 2020
ACS NANO

READ 

Visualization of Charge-Density-Wave Reconstruction and Electronic Superstructure at the Edge of Correlated Insulator $1T\text{-NbSe}_2$

Han Yang, Yeliang Wang, *et al.*

DECEMBER 23, 2021
ACS NANO

READ 

Get More Suggestions >